

Research Paper

Ce_{0.3}Zr_{0.7}O_{1.88}N_{0.12} solid solution as a stable photocatalyst for visible light driven water splitting

Yu Lei Wang^{a,1}, Jia Min Jin^{b,1}, Yu Hang Li^a, Xue Lu Wang^a, Bo Zhang^{c,d}, Xiwen Gong^d, Hai Feng Wang^b, Ai Ping Chen^a, Li Rong Zheng^e, P. Hu^{b,f}, Hua Gui Yang^{a,*}



^a Key Laboratory for Ultrafine Materials of Ministry of Education, School of Materials Science and Engineering, East China University of Science and Technology, 130 Meilong Road, Shanghai 200237, China

^b Key Laboratory for Advanced Materials, Centre for Computational Chemistry and Research Institute of Industrial Catalysis, East China University of Science and Technology, 130 Meilong Road, Shanghai 200237, China

^c State Key Laboratory of Molecular Engineering of Polymers, Department of Macromolecular Science, Fudan University, Shanghai 200438, China

^d Department of Electrical and Computer Engineering, University of Toronto, 35 St George Street, Toronto, Ontario M5S 1A4, Canada

^e Beijing Synchrotron Radiation Facility, Institute of High Energy Physics, Chinese Academy of Sciences, Beijing 100049, China

^f School of Chemistry and Chemical Engineering, The Queen's University of Belfast, Belfast BT9 5AG, UK

ARTICLE INFO

Keywords:

Photocatalysis
Ce_{0.3}Zr_{0.7}O_{1.88}N_{0.12}
Hydrogen evolution
Z-scheme
Stability

ABSTRACT

The search of efficient and stable photocatalysts for the evolution of hydrogen from water using solar energy is of great importance for material science today. Limited by the relatively inferior stability of oxynitrides, the availability of these visible-light-response materials in photocatalysis is still far below what is expected. Here we report a novel oxynitride Ce_{0.3}Zr_{0.7}O_{1.88}N_{0.12} as an efficient and stable H₂-evolving photocatalyst under visible light irradiation, which can further enable overall water splitting by coupling with an O₂-evolving photocatalyst via Z-scheme. Experimental and theoretical results together reveal that the origin of the excellent activity and stability of Ce_{0.3}Zr_{0.7}O_{1.88}N_{0.12} photocatalyst can be attributed to the improved separation rate of photoexcited charge carriers by surface and sub-surface oxygen vacancies. The present study provides a strategy to engineer efficient and stable photocatalysts, and the oxynitride mentioned above could act as a promising candidate of H₂-evolving photocatalyst for designing a prominent Z-scheme photocatalytic system.

1. Introduction

Increasing attention has been drawn towards the search for semiconductors as stable photocatalysts that can efficiently split water under visible light [1,2]. In general, photocatalysts explored so far contain transition-metal ions with d⁰ electronic configuration (e.g., Ti⁴⁺, Nb⁵⁺ and Ta⁵⁺) or typical metal cations of d¹⁰ configuration (e.g., In³⁺, Ga³⁺ and Ge⁴⁺) [3,4]. It is important to note that the tops of the valence bands of metal-oxide photocatalysts with d⁰ or d¹⁰ metal ions usually are derived from O 2p orbitals, thus resulting in wide band-gap semiconductors which cannot operate under visible light [5]. Fortunately, the valence band top can be further upward shifted by introducing N element in metal-oxide photocatalysts, which can be typically attributed to that the nitrogen 2p states are more electropositive than the oxygen 2p states [6]. Thus, a number of oxynitrides such as TaON, BaTaO₂N, Ca₂Ta₃O_{9.7}N_{0.2} and LaTiO₂N have been developed and acted as visible light-response photocatalysts [7–9]. However, most

of these oxynitrides are unstable, presumably due to sluggish charge-carrier separation and fast charge recombination which are induced by significant amounts of bulk defects of these materials through introducing N element [10]. Noteworthily, the bulk defects will introduce trapping and recombination sites for photogenerated electrons and holes, and show degradation effects on the photocatalytic activity and stability [5]. In contrast, surface and sub-surface defects may serve as active sites or trapping sites for photoexcited electrons, thus promoting charge-carrier separation and photocatalytic reaction [11–13]. If the percentage of surface/sub-surface defects is tuned to be relative high, by tailoring the geometric and electronic structures of these materials, the positive influences from surface/sub-surface defects will be powerful enough to overcome the negative effects from bulk defects [14]. Nevertheless, enhancing the density of surface/sub-surface defects to tune oxynitrides into both active and stable photocatalysts still remains as a great challenge.

Herein, we develop a novel solid solution of cerium and zirconia

* Corresponding author.

E-mail address: hgyang@ecust.edu.cn (H.G. Yang).

¹ These authors contributed equally to this work.

nitrogen oxide, $\text{Ce}_{0.3}\text{Zr}_{0.7}\text{O}_{1.88}\text{N}_{0.12}$ (CZON), with abundant surface defects, as an efficient and stable hydrogen evolution photocatalyst under visible light irradiation. Moreover, we present an exceptional result that this material exhibits visible-light-induced overall water splitting through functioning as a building block for H_2 evolution in the artificial heterogeneous Z-scheme photocatalytic systems. Through combination of experimental and theoretical results, we demonstrate that CZON possesses high charge-separation efficiency due to the surface and sub-surface oxygen vacancies, which plays a substantial role in the excellent activity and stability of CZON photocatalyst.

2. Experimental methods

2.1. Synthesis of $\text{Ce}_{0.3}\text{Zr}_{0.7}\text{O}_{1.88}\text{N}_{0.12}$ solid solution

30 mL of aqueous solution containing $\text{Ce}(\text{NO}_3)_3 \cdot 6\text{H}_2\text{O}$ (0.3 m mol), $\text{Zr}(\text{NO}_3)_4 \cdot 5\text{H}_2\text{O}$ (0.7 m mol), GeO_2 (0.5 m mol) and citric acid (0.5 m mol) was put into a 50 mL Teflon container. After stirring for half an hour, the kettle containing the mixture was put in an oven at 200 °C for 24 h. The resulting precipitate was harvested by centrifugation, followed by washing with deionized water for three times and ethanol for three times, and finally dried under vacuum at 60 °C for 12 h. The as-prepared compound was placed at the central part of an alumina tube in a horizontal tube furnace. Then the compound was heated to 880 °C at a rate of 5 °C min⁻¹, keeping at that temperature for 10 h under a NH_3 flow (40 cm³/min) [15]. After cool down, the prepared $\text{Ce}_{0.3}\text{Zr}_{0.7}\text{O}_{1.88}\text{N}_{0.12}$ (CZON) solid solution was collected for further characterizations. For the dispersion of RuO_2 particles on CZON, CZON was impregnated with $\text{Ru}_3(\text{CO})_{12}$ in tetrahydrofuran. Then the products were oxidized in air at 400 °C for 3 h.

2.2. Photocatalytic tests

The photocatalytic decomposition of water using CZON photocatalyst was carried out in a glass gas-closed-circulation system in an Ar atmosphere under irradiation with a 300 W xenon lamp (CEL-HXBF 300). We maintained the temperature of reactant solution at 15 °C by a flow of cooling water during the test. Normally, the H_2 evolution was typically examined in 50 mL of aqueous solution containing 50 mg of CZON and sacrificial electron donors (0.35 M Na_2S -0.25 M Na_2SO_3) [16]. The overall water splitting for Z-scheme photocatalytic systems were performed similarly to H_2 evolution reaction, only changing the reaction solution to NaI solution (1 mM, 50 mL) [17]. Before irradiation, the reaction system was thoroughly degassed by evacuation in order to drive off the air inside. The amounts of H_2 and O_2 produced in the gas phase were monitored by an online gas chromatograph (GC 2014C).

Apparent quantum yield (AQY) value was calculated using the following equation:

AQY(%) = the number of reacted electrons or holes/the number of incident photons × 100 = the number of H_2 molecules × 2/the number of incident photons × 100 or the number of O_2 molecules × 4/the number of incident photons × 100.

2.3. Characterization of catalysts

X-ray powder diffraction (XRD, D/max2550 V) was used for the structural determination. Scanning electron microscopy (SEM), for sample imaging, and electron dispersive X-ray spectroscopy (EDXS), for chemical composition analysis, were recorded using a scanning electron microscope (SEM, JSM-5600 LV). Further microstructural analyses were performed using transmission electron microscope (TEM, JEM 2100F, 200 kV) and a high-resolution transmission electron microscope (HRTEM, JEM 3010, 300 kV). UV diffuse reflectance spectra were recorded using a UV-vis spectrophotometer (Cary 500). The chemical states of the elements in two photocatalytic systems were analyzed

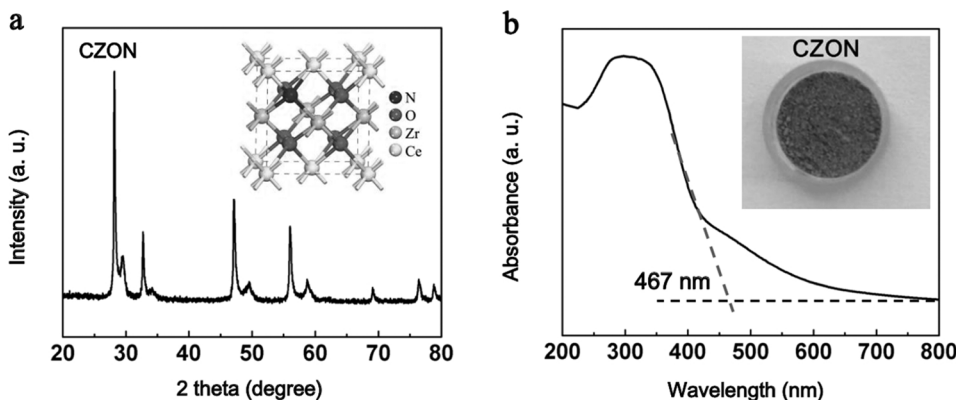
using X-ray photoelectron spectroscopy (XPS, Kratos Axis Ultra DLD, Al K_α radiation), and the binding energy of the C 1 s peak at 284.8 eV was taken as an internal reference. The amount of elements in the sample was measured by ICP-atomic emission spectroscopy (Agilent 725ES) and X-ray fluorescence (XRF) spectroscopy (XRF-1800). The surface area and pore size distribution of catalysts were studied by the Brunauer-Emmett-Teller (BET, ASAS 2460) method. The photoluminescence (PL) spectra were obtained on a Horiba Fluorolog system equipped with a single grating and a time-correlated single photon counting detector. The time-resolved PL spectra were measured using a Fluorolog-3 (HORIBA).

The Ce L₃-edge and Zr K-edge XAFS spectra were measured on the 1W1 B beamline of the Beijing Synchrotron Radiation Facility, China, operated at 2.5 GeV with a typical current of 200 mA. Zr foil, CeO_2 and ZrO_2 were used as reference samples and measured in the transmission mode, and the initial and used CZON photocatalysts were measured in fluorescence mode. We used IFEFFIT software to calibrate the energy scale, to correct the background signal and to normalize the intensity.

2.4. Model and density functional theory calculation methods

CeO_2 exists in the cubic fluorite structure, which consists of a cubic array of 4-fold-coordinated oxygen ions and metal ions occupying half of the 8-fold-coordinated cationic sites (Fig. S11a) [18]. For ZrO_2 , the cubic fluorite was also utilized (Fig. S11b). To be consistent with the work in the paper, the lattice substituting model was used to model the $\text{Ce}_{1-x}\text{Zr}_x\text{O}_2$: In the primitive cell containing four CeO_2 units, two of the four Ce^{4+} were substituted with Zr^{4+} to represent $\text{Ce}_{0.5}\text{Zr}_{0.5}\text{O}_2$ (Fig. S11c), and one of the eight O atoms was replaced by N to simulate the CZON (Fig. S11d), namely the CZON catalysts used in the experiment. Lattice constants for each of these structures were optimized.

All the spin-polarised calculations were performed with the Perdew-Burke-Ernzerhof (PBE) functional within the generalised gradient approximation as implemented in the VASP package [19–21]. The project-augmented wave (PAW) method was used to represent the core-valence electron interaction [22]. To correctly describe the localization of 4f electrons, the so-called DFT + U methodology has been extensively used for ceria and it has been already shown that the approach can accurately reproduce the electronic and structural properties of CeO_2 [23,24]. We used a plane-wave cutoff energy of 500 eV and applied a $8 \times 8 \times 8$ Monkhorst-Pack k -point mesh for the unit cell of ($1 \times 1 \times 1$) with Gaussian smearing of 0.05 eV. The $\text{CeO}_2(111)$, $\text{ZrO}_2(111)$, $\text{Ce}_{0.5}\text{Zr}_{0.5}\text{O}_2(111)$ and CZON(111) surface were all modeled as a periodic slab with 12 atomic layers, consisting of 4 O-Ce/Zr-O trilayers and the vacuum between slabs was ~15 Å. A p(2×4) surface cell which is rather large ($7.75 \times 13.42 \text{ \AA}^2$) with corresponding $2 \times 1 \times 1$ k -point mesh was used in order to fully take the relaxation effects into account. The transition states (TS) were searched using a constrained optimization scheme [25]. The TSs can be located via changing the fixed distance and was verified when (i) all forces on atoms are small (the criterion is set as 0.05 eV/Å), and (ii) the total energy is a maximum along the reaction coordination but a minimum with respect to the rest of the degrees of freedom [26,27]. The formation energy of the O vacancy was calculated as follows: $E_f = E[\text{Ce}_{1-x}\text{Zr}_x\text{O}_{2-8}] - E[\text{Ce}_{1-x}\text{Zr}_x\text{O}_2] + 1/2E[\text{O}_2]$, in which $E[\text{Ce}_{1-x}\text{Zr}_x\text{O}_{2-8}]$, $E[\text{Ce}_{1-x}\text{Zr}_x\text{O}_2]$, and $E[\text{O}_2]$ are the energies of $\text{Ce}_{1-x}\text{Zr}_x\text{O}_{2-8}$ (reduced $\text{Ce}_{1-x}\text{Zr}_x\text{O}_2$ surface), clean $\text{Ce}_{1-x}\text{Zr}_x\text{O}_2$, and gas-phase O_2 , respectively. The adsorption energy of H_2O molecule on the reduced $\text{Ce}_{1-x}\text{Zr}_x\text{O}_2$ surface is defined as: $E_{ads}(\text{H}_2\text{O}) = E(\text{sur}) + E(\text{H}_2\text{O}) - E(\text{H}_2\text{O}/\text{sur})$, where $E(\text{sur})$, $E(\text{H}_2\text{O})$ and $E(\text{H}_2\text{O}/\text{sur})$ are the energies of the reduced catalyst surface, H_2O in the gas phase, and H_2O adsorbed on the reduced catalyst surface, respectively. The more positive $E_{ads}(\text{H}_2\text{O})$ is, the more strongly the H_2O molecule binds with the reduced surface.



3. Results and discussion

3.1. Crystal structure and composition

This new photocatalyst CZON was synthesized through a two-step route. The intermediates CeGeO_4 and Zr_3GeO_8 (Fig. S1) were formed by a hydrothermal process; then after heat treatment in a gaseous ammonia atmosphere, the white intermediates were changed to yellow-green resultant CZON. Noteworthily, the weight of samples decreased after heat and nitridation treatment, which is attributed to that Ge^{4+} ions are reduced into Ge^{2+} and the Ge^{2+} ions may be gasified as GeO when the temperature achieves the boiling point of GeO (710°C) [15]. The elemental analysis of CZON is shown in Table S1. In the sample CZON, the O/N atom ratio was approximately 7.478, while the ratio of Ce to Zr was close to 3:7. Therefore, the ideal composition of the as-synthesized samples can be expressed as $\text{Ce}_{0.3}\text{Zr}_{0.7}\text{O}_{1.88}\text{N}_{0.12}$, although the real compositions somewhat diverge from the ideal one. The proposed crystal structure of the CZON is schematically shown in Fig. 1a inset. It is clear to see that the O/N atom is connected by Ce atoms and Zr atoms, forming a cubic structure. X-ray diffraction (XRD) patterns of final product confirmed this crystal structure (Fig. 1a) [28,29]. The UV-vis diffuse reflectance spectrum (Fig. 1b) displays that the absorption edge of synthesized CZON is located at 467 nm, therefore, the band gap of the sample CZON is determined to be 2.76 eV. Fig. S2 shows the band structure of CZON, along with CeO_2 and ZrO_2 data for comparison. In addition, a schematic illustration of the calculated band edges for ZrO_2 , CeO_2 and CZON is presented in Fig. S3, showing the smallest bandgap for CZON, which is in good accordance with our experimental findings, and, in principle, indicating the potential of CZON as a photocatalyst for water splitting under visible-light irradiation.

3.2. Morphology and inner crystal structures

The morphology and structure details of the synthesized CZON samples were investigated by scanning electron microscope (SEM) and transmission electron microscopy (TEM) measurements. SEM images (Fig. S4) reveal that the prepared CZON contains broad distribution of sphere sizes. Energy dispersive X-ray (EDX) mapping spectroscopy analysis (Fig. 2a–e) for an individual CZON nanosphere reveals that the elements of Ce, Zr, O and N are distributed throughout the nanosphere. In addition, it can be seen that a series of nanoparticles with mean particle size of about 12.9 nm aggregate to a big nanosphere in the TEM images (Fig. 2f, Fig. S5). The high-resolution (HR)TEM image (Fig. 2g) displays the lattice fringes of 0.31 nm, and the value can be attributed to the {111} crystal planes [30]. Selected area electron diffraction patterns show four brilliant rings, which can be indexed to the {111}, {200}, {220} and {311} crystal planes, respectively [31]. The Brunauer-Emmett-Teller (BET) surface area of the CZON is up to $29.67 \text{ m}^2 \text{ g}^{-1}$, which is much larger than that of the sample ZrO_2 ($3.93 \text{ m}^2 \text{ g}^{-1}$) or CeO_2 ($2.61 \text{ m}^2 \text{ g}^{-1}$).

3.3. Electronic structure

Raman spectroscopy, X-ray photoelectron spectroscopy (XPS) and X-ray absorption fine structure (XAFS) measurements were used to further clarify the structural information of CZON. Raman spectrum of CZON shows a slightly red-shifted peak of 463.5 cm^{-1} as well as its reduced intensity compared with the spectrum of CeO_2 , which is attributed to the photon-confinement effects induced by defects [5]. Two additional weak peaks appear at around 261.5 cm^{-1} and 632.2 cm^{-1} due to the presence of defects, which are mainly ascribed to oxygen vacancies (Fig. 3a) [32]. Fig. S6 displays the XPS spectra for Ce 3d, Zr 3d, O 1s and N 1s in sample CZON (see Supplementary Note 1 for details). In the O 1s XPS spectra (Fig. 3b), the binding energy values of 529.7 and 531.2 eV are attributed to lattice oxygen and surface bridging hydroxyls (OH species), respectively. CZON exhibits a strong peak shape at 531.2 eV, revealing abundant oxygen defects on the surface [5,33]. Correspondingly, the formation of oxygen vacancy is accompanied by localization of the electrons left behind in Ce 4f states, leading to formation of two Ce^{3+} ions [34]. The increased Ce^{3+} species in CZON were confirmed by XPS spectra of Ce 3d (Fig. S7). In addition, CZON with numerous Ce^{3+} ions was further investigated through the XAFS spectra (Fig. S8, see Supplementary Note 2 for details). Therefore, the existence of abundant oxygen vacancies on the surface of CZON could be clearly revealed.

3.4. Photocatalytic tests

Then, the typical reaction for H_2 production was performed to evaluate the photocatalytic performance of CZON sample. For these experiments, 50 mg of the as-prepared sample CZON without cocatalyst was dispersed in 50 mL of $\text{Na}_2\text{S}-\text{Na}_2\text{SO}_3$ solution. As shown in Fig. 4a, continuous H_2 evolution without noticeable degradation was observed throughout the experiment with intermittent evacuation every 24 h. The total production of H_2 after 24 h was 19 μmol and 101.7 μmol under visible light ($\lambda > 420 \text{ nm}$) and UV-vis light ($\lambda > 300 \text{ nm}$) irradiation, respectively. In addition, it was apparent to find that no noticeable decrease in the activity can be observed even after storage in the reactor for as long as 15 days. Nitrogen evolution was negligible through the illumination onset. Combined with the results mentioned in supplementary material (Fig. S9 and Table S2), excellent stability of CZON can be confirmed. The apparent quantum yield of CZON was approximately 0.057% at 435 nm and 3.37% at 365 nm.

Furthermore, we demonstrate an exceptional result that CZON photocatalyst functions as a building block for H_2 evolution in the Z-scheme photocatalytic systems. As displayed in Table S3, no H_2 or O_2 could be tested using the 1.0 mol% Pt loaded WO_3 catalyst, and only H_2 could be detected over 2.0 mol% RuO_2 loaded CZON in aqueous NaI solution. However, both H_2 and O_2 could be achieved with a H_2/O_2 ratio close to 2.0 when the samples RuO_2/CZON and Pt/WO_3 were added into 1.0 mM NaI solution (Fig. 4b). Of note, the H_2 evolution rate

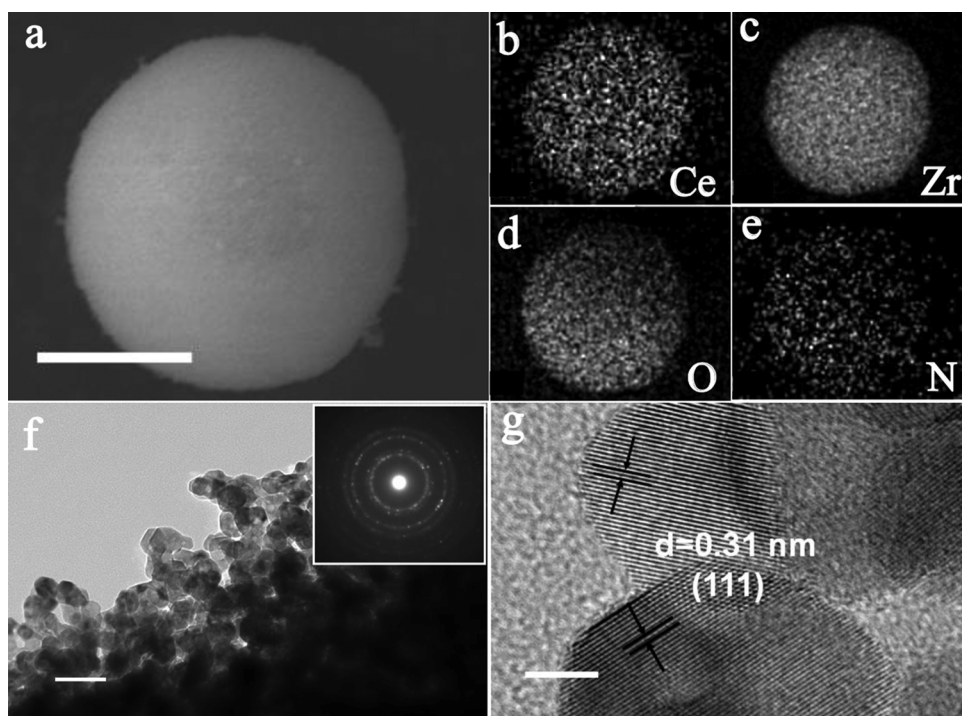


Fig. 2. (a) FESEM images of CZON and (b) Ce (blue), (c) Zr (light blue), (d) O (green), (e) N (red). (f, g) (HR)TEM images of CZON photocatalyst. The corresponding SAED pattern is shown in the inset. The scale bars in panels (a), (f) and (g) are 2 μ m, 50 nm and 5 nm, respectively. CZON: $\text{Ce}_{0.3}\text{Zr}_{0.7}\text{O}_{1.88}\text{N}_{0.12}$. (For interpretation of the references to colour in this figure legend, the reader is referred to the web version of this article.)

for overall water splitting in the Z-scheme photocatalytic systems is about 2 times compared to that for the half reaction under UV-vis light irradiation (Table S3). As shown in Fig. 4c, RuO₂/CZON, as well as Pt/WO₃, can absorb of photons to form electron-hole pairs. The photo-generated electrons at Pt/WO₃ move to the valence band of RuO₂/CZON through the electron mediator. Therefore, more photogenerated electrons at RuO₂/CZON participated in the reduction of H₂O due to the lower probability of electrons and holes recombination, resulting in enhancement of H₂ evolution rate.

3.5. Charge separation efficiency

To understand the mechanism of photocatalytic reaction, we first examined the possible influence of oxygen vacancies on the charge separation efficiency. The sample CZON with more surface defects than CeO₂ has been revealed by the structure characterizations mentioned above. Unlike samples CZON and CeO₂, ZrO₂ has few both bulk and surface defects. As shown in Fig. 5a, the photoluminescence (PL) intensity of ZrO₂ was the weakest compared to those of CeO₂ and CZON, indicating that bulk defects introduce recombination sites for photo-generated electrons and holes [35]. Meanwhile, the PL intensity of CZON was weaker than that of CeO₂, which could be attributed to the

high charge separation efficiency of CZON, suggesting that surface defects contribute to charge-carrier separation. These observations indicate that bulk defects will introduce trapping and recombination sites for photogenerated electrons and holes, while surface and sub-surface oxygen vacancies contribute to charge-carrier separation for photocatalytic reaction [5]. This argument is also supported by the time-resolved PL spectroscopy results. Fig. 5b displays the PL emission decay profiles expressed by bi-exponential fitting, indicating that PL decay occurred through two relaxation pathways (Table S4). The mean amplitude-weighted average exciton lifetimes (τ_{ave}) are determined to be 0.484, 0.335 and 0.227 ns for ZrO₂, CeO₂ and CZON, respectively. In comparison with ZrO₂, both CeO₂ and CZON exhibit acceleration of PL decay kinetics, which should be attributed to the opening of an additional channel for photogenerated electrons to transfer to the new trap states oxygen vacancies. In addition, the separation of the photoexcited carriers was dramatically promoted, as the new trap states oxygen vacancies on the surface can help more photoexcited electrons to transfer to reactant H₂O. More importantly, the comparison between CeO₂ and CZON clearly suggests that a more efficient charge separation can be obtained in the latter.

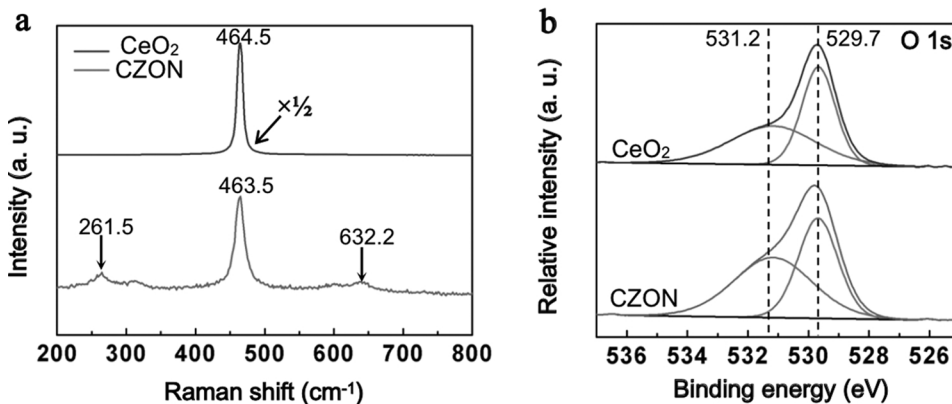


Fig. 3. (a) Raman spectra of the CeO₂ and CZON photocatalysts. $\frac{1}{2}$: The Intensity of the peak is reduced to half of the original. (b) O 1s XPS of the CeO₂ and CZON photocatalysts. CZON: $\text{Ce}_{0.3}\text{Zr}_{0.7}\text{O}_{1.88}\text{N}_{0.12}$.

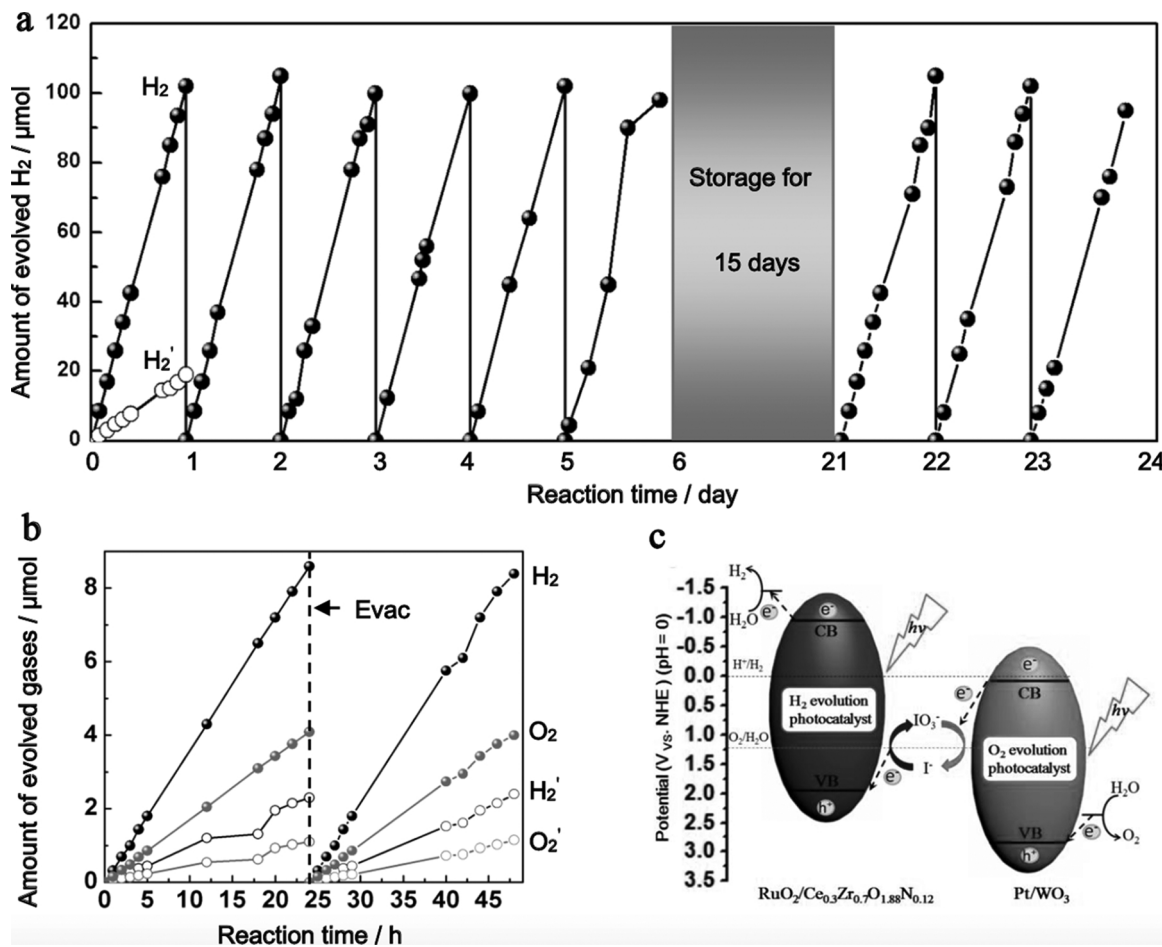


Fig. 4. (a) Photocatalytic H₂ evolution performance for CZON sample (50 mg) in a 0.35 M Na₂S and 0.25 M Na₂SO₃ solution under UV-vis irradiation ($\lambda > 300$ nm, H₂) or visible-light irradiation alone ($\lambda > 420$ nm, H₂'). (b) Dependence of the rates of H₂ and O₂ evolution over a mixture of RuO₂/CZON and Pt/WO₃ under UV-vis (H₂, O₂) or visible-light irradiation alone (H₂', O₂'). Reaction conditions: catalyst, 50 mg of RuO₂/CZON and 50 mg of Pt/WO₃; 1 mM NaI solution, 50 mL. (c) Plasmonic Z-scheme mechanism of the RuO₂/CZON and Pt/WO₃ systems. CZON: Ce_{0.3}Zr_{0.7}O_{1.88}N_{0.12}.

3.6. Density functional theory calculation

Furthermore, to probe more insight into the mechanism of photocatalytic reaction, first-principle calculations were conducted to examine the electronic structure of CZON and its catalytic activity in promoting water splitting. Firstly, the electronic structure analysis demonstrated that light harvest of CZON can indeed be enhanced owing to the introduction of nitrogen element. As seen from the density of

states (DOS) in Fig. 6a and b, the O-2p and Ce-f (Zr-d) states mainly contribute to the valence band and conduction band, respectively, for the CeO₂ (ZrO₂) system. Also, we examined the DOS for the solid solution Ce_{0.5}Zr_{0.5}O₂ (CZO, Fig. S10) without the addition of N ingredient, and little change about the valence band maximum (VBM) in comparison with CeO₂ and ZrO₂ was observed. By contrast, for the CZON material, with the involvement of N, the N-2p state evidently contributes to the VBM due to the formation of Ce-N and Zr-N bonds

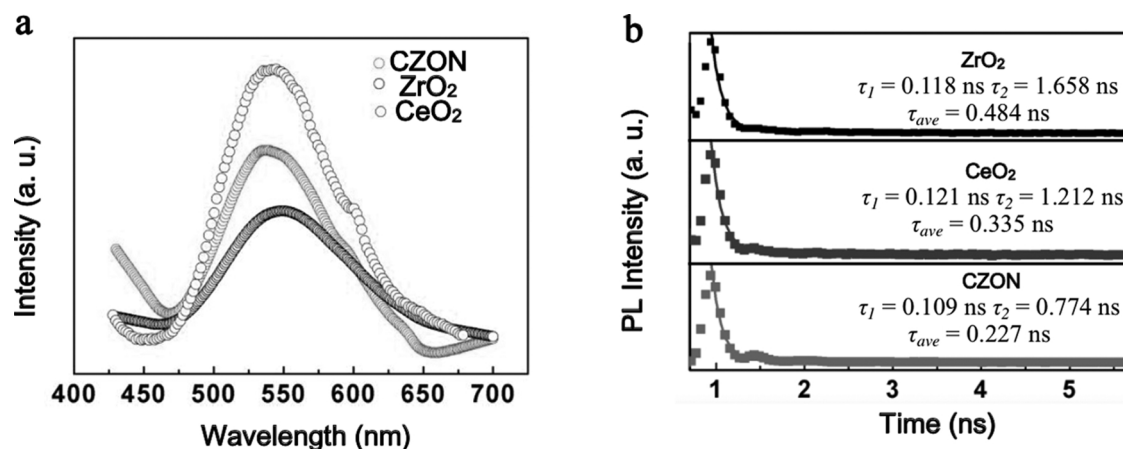


Fig. 5. (a) PL spectra of samples ZrO₂, CeO₂ and CZON. (b) PL decay profiles of ZrO₂, CeO₂ and CZON. CZON: Ce_{0.3}Zr_{0.7}O_{1.88}N_{0.12}.

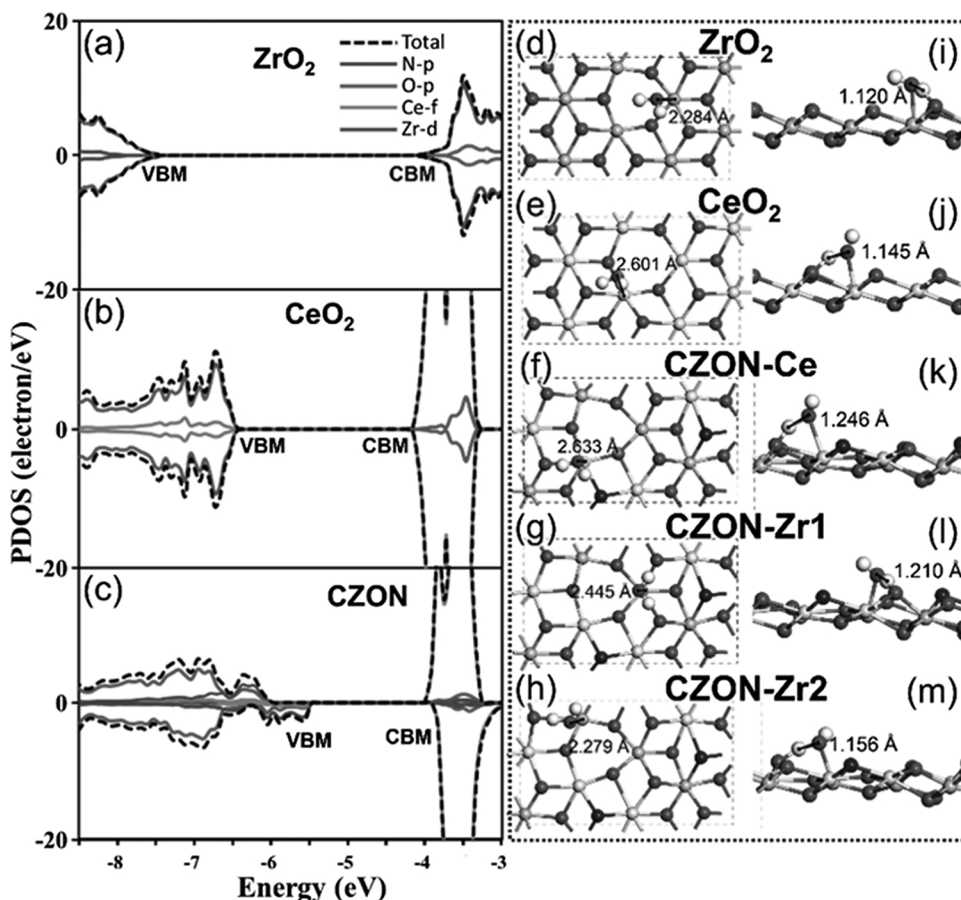


Fig. 6. The projected density of states (PDOS) of bulk ZrO_2 , CeO_2 and CZON (a–c). To better uncover the origin of the bandgap variation, all the energy levels are aligned to the vacuum level. (d–m) show the optimized structures of the H_2O adsorption (d–h) and dissociation transition state (i–m) on $\text{CeO}_2(111)$, $\text{ZrO}_2(111)$ and CZON(111) surface (f–h denote the adsorption at Ce^{4+} , Zr1 and Zr2; k–m are the corresponding dissociation transition state). The length values in (d–h) represent the distance between the reaction site and the O atom of H_2O , and those in (i–m) represent the O–H bond of H_2O at the dissociation transition state. CZON: $\text{Ce}_{0.3}\text{Zr}_{0.7}\text{O}_{1.88}\text{N}_{0.12}$.

(Fig. 6c), resulting in the shift of VBM towards the high-energy-level direction, which accordingly narrow the bandgap of CZON.

Secondly, to understand the excellent catalytic activity of CZON, we extensively calculated and compared the formation of oxygen vacancies, as well as the consequent H_2O adsorption and dissociation on CeO_2 , ZrO_2 and CZON, which are expected to be crucial processes for the whole water splitting reaction [36,37]. The most stable (111) surfaces, with three-coordinated lattice oxygen (O_{3c}) exposed as the main reaction sites, were chosen as the substrates. The calculations indicate that the surface and subsurface oxygen vacancies are more inclined to form on CZON surface, rather than on $\text{CeO}_2(111)$ and $\text{ZrO}_2(111)$ surface (Table S5), being good accordance with the experimental observation that CZON has a richer O vacancy concentration in the surface and subsurface region. Moreover, we further explore the activity of CZON on H_2O adsorption and dissociation (Table S6). Based on our calculations, we can see that the H_2O at the oxygen vacancy can considerably adsorb at the nearest Ce^{4+} or Zr^{4+} sites on the reduced CZON(111) surfaces, giving the adsorption energies of 0.61 eV for Ce^{4+} site and 0.68/0.55 eV for the two Zr^{4+} sites. More importantly, these adsorbed H_2O molecules can readily dissociate by releasing one H to the adjacent lattice O and the OH refilling the O vacancy (Fig. 6k–m), corresponding to the barriers as low as 0.16 eV (Ce^{4+}) and 0.01/0.15 eV (Zr^{4+}), respectively; also, the whole processes are exothermic (-0.38 , -0.31 / -0.44 eV). Therefore, we can realize that the defective CZON(111) is catalytically active for activating H_2O dissociation in terms of both thermodynamics and kinetics. For comparison, the performance of H_2O dissociation on the reduced CeO_2 and ZrO_2 was also examined; the adsorption energies of H_2O are calculated to be 1.15 and 0.82 eV, respectively, and the corresponding dissociation barrier are 0.01 and 0.17 eV, indicating that both reduced oxides are inherently capable of dissociating H_2O , but it needs to be emphasized that the overall activity would be limited by their large bandgap and high formation energy of

oxygen vacancy (low oxygen vacancy concentration). Please see Fig. 6 for all the optimized adsorption configurations and dissociation transition state of H_2O .

4. Conclusions

In conclusion, CZON as a novel visible-light-responsive photocatalyst has demonstrated its excellent stability and activity for H_2 evolution. Employing it as an efficient photocatalyst for H_2 evolution even without a cocatalyst, we achieved apparent quantum efficiencies of 0.057% at 435 nm and 3.37% at 365 nm, respectively. In addition, overall water splitting with simultaneous H_2 and O_2 evolution has been obtained in the Z-scheme photocatalytic systems, with RuO_2/CZON and Pt/WO_3 as H_2 -evolving and O_2 -evolving photocatalyst, respectively. Meanwhile, we demonstrate that the excellent stability and activity of CZON can be attributed to that surface and sub-surface oxygen vacancies of CZON contribute to charge-carrier separation for photocatalytic reaction. This novel photocatalyst may serve as H_2 -evolving photocatalyst for designing of numerous Z-scheme photocatalytic systems, which are active under visible light irradiation for overall water splitting.

Author contributions

The manuscript was written through contributions of all authors. All authors have given approval to the final version of the manuscript.

Notes

The authors declare no competing financial interests.

Acknowledgments

This work was financially supported by National Natural Science Foundation of China (21503079, 21333003, 21573068, 21603073 and 91534202), SRF for ROCS, SEM, Program of Shanghai Subject Chief Scientist (15XD1501300), Shu-Guang project (13SG30), Fundamental Research Funds for the Central Universities (WJ1616007, 222201718002, 222201514303 and 222201714001), China Postdoctoral Science Foundation Funded Project (2016M591615, 2017T100276 and 2016M601523), National Postdoctoral Program for Innovative Talents (BX201600050), “Chen Guang” project supported by Shanghai Municipal Education Commission and Shanghai Education Development Foundation (16CG31 and <gn4>13CG24</gn41>), Shanghai Sailing Program (17YF1402900), Science and Technology Commission of Shanghai Municipality (14JC1490900). The authors also thank the crew of 1W1B beamline of Beijing Synchrotron Radiation Facility for the constructive assistance in the XAFS measurements and data analyses.

Appendix A. Supplementary data

Supplementary data associated with this article can be found, in the online version, at <http://dx.doi.org/10.1016/j.apcatb.2017.11.012>.

References

- [1] T.J. Meyer, *Nature* 451 (2008) 778–779.
- [2] H. Fujito, H. Kunioku, D. Kato, H. Suzuki, M. Higashi, H. Kageyama, R. Abe, *J. Am. Chem. Soc.* 138 (2016) 2082–2085.
- [3] X. Wang, K. Maeda, A. Thomas, K. Takanabe, G. Xin, J.M. Carlsson, K. Domen, M. Antonietti, *Nat. Mater.* 8 (2009) 76–80.
- [4] K. Maeda, T. Takata, M. Hara, N. Saito, Y. Inoue, H. Kobayashi, K. Domen, *J. Am. Chem. Soc.* 127 (2005) 8286–8287.
- [5] L. Li, J. Yan, T. Wang, Z.J. Zhao, J. Zhang, J. Gong, N. Guan, *Nat. Commun.* 6 (2015) 5881.
- [6] S. Chen, Y. Qi, T. Hisatomi, Q. Ding, T. Asai, Z. Li, S.S.K. Ma, F. Zhang, K. Domen, C. Li, *Angew. Chem. Int. Ed.* 54 (2015) 8498–8501.
- [7] R. Abe, M. Higashi, K. Domen, *J. Am. Chem. Soc.* 132 (2010) 11828–11829.
- [8] M. Higashi, K. Domen, R. Abe, *J. Am. Chem. Soc.* 135 (2013) 10238–10241.
- [9] K. Maeda, M. Higashi, B. Siritanaratkul, R. Abe, K. Domen, *J. Am. Chem. Soc.* 133 (2011) 12334–12337.
- [10] J. Sato, N. Saito, Y. Yamada, K. Maeda, T. Takata, J.N. Kondo, M. Hara, H. Kobayashi, K. Domen, Y. Inoue, *J. Am. Chem. Soc.* 127 (2005) 4150–4151.
- [11] J. Paier, C. Penschke, J. Sauer, *Chem. Rev.* 113 (2013) 3949–3985.
- [12] Y. Li, Z. Wei, F. Gao, L. Kovarik, R.A.L. Baylon, C.H.F. Peden, Y. Wang, *ACS Catal.* 5 (2015) 3006–3012.
- [13] X. Chen, L. Liu, P.Y. Yu, S.S. Mao, *Science* 331 (2011) 746–750.
- [14] Y.H. Li, P.F. Liu, L.F. Pan, H.F. Wang, Z.Z. Yang, L.R. Zheng, P. Hu, H.J. Zhao, L. Gu, H.G. Yang, *Nat. Commun.* 6 (2015) 8064.
- [15] J. Xing, H.F. Wang, C. Yang, D. Wang, H.J. Zhao, G.Z. Lu, P. Hu, H.G. Yang, *Angew. Chem. Int. Ed.* 51 (2012) 3611–3615.
- [16] A. Ishikawa, T. Takata, J.N. Kondo, M. Hara, H. Kobayashi, K. Domen, *J. Am. Chem. Soc.* 124 (2002) 13547–13553.
- [17] K. Maeda, M. Higashi, D. Lu, R. Abe, K. Domen, *J. Am. Chem. Soc.* 132 (2010) 5858–5868.
- [18] H.F. Wang, X.Q. Gong, Y.L. Guo, Y. Guo, G.Z. Lu, P. Hu, *J. Phys. Chem. C* 113 (2009) 10229–10232.
- [19] J.P. Perdew, K. Burke, M. Ernzerhof, *Phys. Rev. Lett.* 77 (1996) 3865.
- [20] G. Kresse, J. Furthmüller, *Phys. Rev. B* 54 (1996) 11169.
- [21] G. Kresse, J. Furthmüller, *Comput. Mater. Sci.* 6 (1996) 15–50.
- [22] G. Kresse, D. Joubert, *Phys. Rev. B* 59 (1999) 1758.
- [23] V.V. Pushkarev, V.I. Kovalchuk, J.L. d’Itri, *J. Phys. Chem. B* 108 (2004) 5341–5348.
- [24] Y.M. Choi, H. Abernathy, H.T. Chen, M.C. Lin, M. Liu, *ChemPhysChem* 7 (2006) 1957–1963.
- [25] A. Alavi, P. Hu, T. Deutsch, P.L. Silvestrelli, J. Hutter, *Phys. Rev. Lett.* 80 (1998) 3650.
- [26] Z.P. Liu, P. Hu, *J. Am. Chem. Soc.* 124 (2002) 14770–14779.
- [27] Z.P. Liu, P. Hu, *J. Am. Chem. Soc.* 125 (2003) 1958–1967.
- [28] S. Shao, A.W. Shi, C.L. Liu, R.Z. Yang, W.S. Dong, *Fuel Process. Technol.* 125 (2014) 1–7.
- [29] J.O. Shim, D.W. Jeong, W.J. Jang, K.W. Jeon, B.H. Jeon, S.Y. Cho, H.S. Roh, J.G. Na, C.H. Ko, Y.K. Oh, S.S. Han, *Renew. Energy* 65 (2014) 36–40.
- [30] X. Liang, X. Wang, Y. Zhuang, B. Xu, S. Kuang, Y. Li, *J. Am. Chem. Soc.* 130 (2008) 2736–2737.
- [31] A.M. Arias, M.F. García, V. Ballesteros, L.N. Salamanca, J.C. Conesa, C. Otero, J. Soria, *Langmuir* 15 (1999) 4796–4802.
- [32] R. Verma, S.K. Samdarshi, S. Bojja, S. Paul, B. Choudhury, *Sol. Energ. Mat. Sol. C.* 141 (2015) 414–422.
- [33] K. Zhang, L. Wang, J.K. Kim, M. Ma, G. Veerappan, C.L. Lee, K. Kong, H. Lee, J.H. Park, *Energy Environ. Sci.* 9 (2016) 499–503.
- [34] J. Paier, C. Penschke, J. Sauer, *Chem. Rev.* 113 (2013) 3949–3985.
- [35] J.D. Xiao, Q. Shang, Y. Xiong, Q. Zhang, Y. Luo, S.H. Yu, H.L. Jiang, *Angew. Chem. Int. Ed.* 128 (2016) 9535–9539.
- [36] Z. Lin, J. Xiao, L. Li, P. Liu, C. Wang, G. Yang, *Adv. Energy Mater.* 6 (2016) 1501865.
- [37] K. Shirai, T. Sugimoto, K. Watanabe, M. Haruta, H. Kurata, Y. Matsumoto, *Nano Lett.* 16 (2016) 1323–1327.